Tropical Atlantic multidecadal variability is dominated by external forcing

https://doi.org/10.1038/s41586-023-06489-4

Received: 7 February 2023

Accepted: 27 July 2023

Published online: 13 September 2023



Check for updates

Chengfei He^{1⊠}, Amy C. Clement¹, Sydney M. Kramer², Mark A. Cane³, Jeremy M. Klavans², Tyler M. Fenske¹ & Lisa N. Murphy¹

The tropical Atlantic climate is characterized by prominent and correlated multidecadal variability in Atlantic sea surface temperatures (SSTs), Sahel rainfall and hurricane activity¹⁻⁴. Owing to uncertainties in both the models and the observations, the origin of the physical relationships among these systems has remained controversial³⁻⁷. Here we show that the cross-equatorial gradient in tropical Atlantic SSTs-largely driven by radiative perturbations associated with anthropogenic emissions and volcanic aerosols since 1950^{3,7}—is a key determinant of Atlantic hurricane formation and Sahel rainfall. The relationship is obscured in a large ensemble of CMIP6 Earth system models, because the models overestimate long-term trends for warming in the Northern Hemisphere relative to the Southern Hemisphere from around 1950 as well as associated changes in atmospheric circulation and rainfall. When the overestimated trends are removed, correlations between SSTs and Atlantic hurricane formation and Sahel rainfall emerge as a response to radiative forcing, especially since 1950 when anthropogenic aerosol forcing has been high. Our findings establish that the tropical Atlantic SST gradient is a stronger determinant of tropical impacts than SSTs across the entire North Atlantic, because the gradient is more physically connected to tropical impacts via local atmospheric circulations⁸. Our findings highlight that Atlantic hurricane activity and Sahel rainfall variations can be predicted from radiative forcing driven by anthropogenic emissions and volcanism, but firmer predictions are limited by the signal-to-noise paradox 9-11 and uncertainty in future climate forcings.

Basin-scale multidecadal fluctuations in sea surface temperatures (SSTs) in the Atlantic (AMV), along with associated impacts such as Sahel rainfall^{2,12}. North Atlantic hurricanes¹⁻⁴ (NAHs) and the European and North American summer climate¹³, are components of a multifaceted mode we will refer to as Atlantic multidecadal climate variability (AMCV). Simulating and understanding the historical evolution of the observed AMCV is vital to making successful predictions for short- and long-term adaptation. Here we study the tropical AMCV over the last century using a grand ensemble of historical simulations (46 models and approximately 400 realizations; Supplementary Table 1) from the Coupled Model Intercomparison Project 6 (CMIP6). We attribute the influence of greenhouse gases (GHGs), natural radiative forcings (NAT), anthropogenic aerosols (AER) and internal variability on the tropical AMCV.

A spurious trend from 1950 in CMIP6 runs

We first compare observations with data from CMIP6 simulations for June-October (JJASO) for North Atlantic SSTs, Sahel rainfall and vertical wind shear (VWS, a key feature of the environment in which NAHs form) over the main development region (MDR; 80-20° W, 10-20 °N) (see 'Definitions' in Methods). We focus on the boreal summer season as it is the most relevant for tropical impacts. Recent research has highlighted the signal-to-noise paradox, in which the forced signal in models is comparatively weaker than the internal noise compared to real-world observations 9-11. To compensate for the low signal-to-noise ratio, we normalize the time series for both the models and the observations. Figure 1a shows that the forced North Atlantic SSTs, as estimated by the CMIP6 ensemble mean (see 'Definitions' in Methods), agrees reasonably well with the observations. The SSTs are characterized by a largely linear warming trend. By contrast, the long-term behaviour of the forced Sahel rainfall and VWS diverge considerably from the observations. The modelled Sahel rainfall generally exhibits an increasing trend like the simulated North Atlantic SSTs, whereas the observed data has multidecadal variability before the 1950s and a pronounced drying trend between the 1950s and 1980s, followed by a recovery (Fig. 1b). Although the simulated VWS has a negative trend, the observed VWS has a similar multidecadal time history as the observed Sahel rainfall (Fig. 1c). The differences between the simulated and observed values are represented by the grey curves, which all have a linear trend since 1950. This is most evident for Sahel rainfall and VWS, but also visible for North Atlantic SSTs (Fig. 1a-c). This spurious linear trend is not

Rosenstiel School of Marine, Atmospheric, and Earth Science, University of Miami, FL, USA. 2Department of Atmospheric and Oceanic Sciences, University of Colorado, Boulder, CO, USA. ³Lamont-Doherty Earth Observatory of Columbia University, Palisades, NY, USA. [™]e-mail: cxh1079@miami.edu

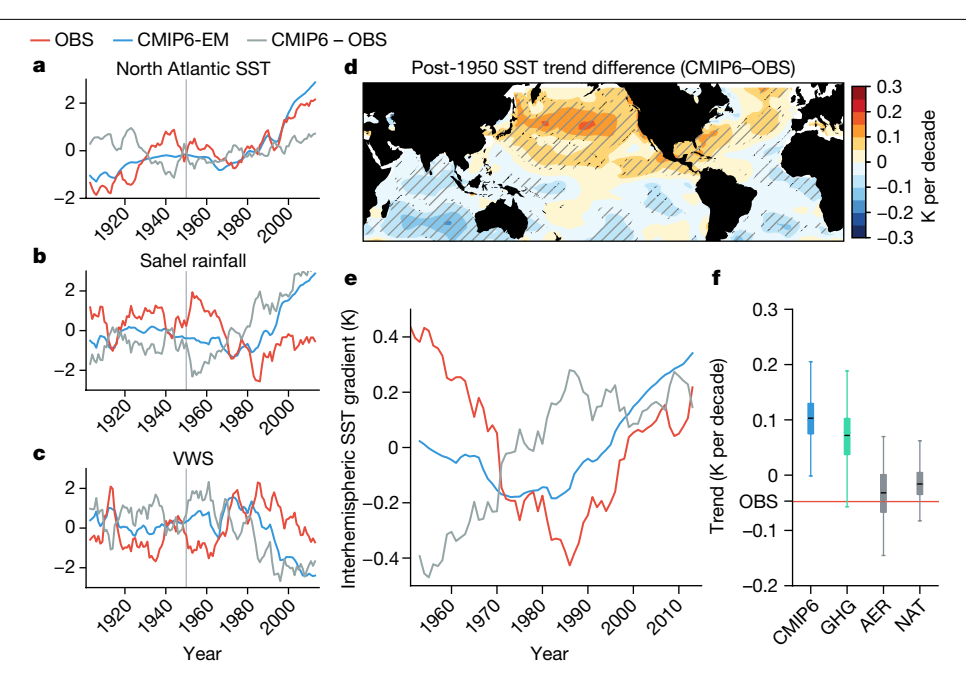


Fig. 1| **Systemic model-data differences due to the interhemispheric SST contrast. a-c**, Ensemble means (EM) for a large dataset from CMIP6 model simulations (blue) and observations (OBS; red) for indices for the boreal summer (JJASO) for 1900–2014. Observations and simulated data are not detrended but are normalized to the unit variance to allow comparison with the anaemic signal in the models. The grey curves are the differences between the two. North Atlantic SSTs (a), Sahel rainfall (b) and VWS (c) in the MDR are shown. d, Differences in the SST trends for JJASO from 1950 to 2014 between the CMIP6 ensemble means and observations. Regions of statistical significance at the

99% confidence level according to Student's *t*-test are hatched. The map was plotted using the cartopy package in Python. **e**, Simulated and observed interhemispheric SST gradients and their differences from 1950 to 2014. Observations and simulated data are neither detrended nor normalized, although climatologies have been removed. **f**, Box plots of the interhemispheric SST contrast trends for CMIP6, DAMIP and observation data (red). The inner box runs from the first to the third quantile, whereas the whiskers denote the 10% and 90% percentiles. The black dot in the box is the average. A five-year running mean is applied to the time series in **a**-**c** and **e** for presentation.

restricted to the Atlantic basin but is also seen in rainfall related to the Indian and East Asian monsoons, the position of the intertropical convergence zone and rainfall over the continental United States (Extended Data Fig. 1a,b).

We argue that the post-1950 model-data differences for atmospheric circulation and rainfall are due to differences in the interhemispheric SST gradient (see 'Definitions' in Methods). Figure 1d shows the differences in the simulated SST trends compared to observations for the global ocean. The hemispheric differences in the SST trend imply that the modelled ocean surface in the Northern Hemisphere warmed faster than observations but slower than observations in the Southern Hemisphere. This interhemispheric SST gradient is further quantified in Fig. 1e. The observed interhemispheric SST gradient has no clear trend but, rather, shows strong multidecadal variability¹⁴. The modeldata differences for the SST gradients also show a linear trend, with the model predicting more warming for the Northern Hemisphere compared to the Southern Hemisphere than has been observed (Fig. 1e, grey curve). The correlations between the grey curves in Fig. 1e and Fig. 1b,c are around 0.9 (DOF = 12 and P < 0.0001), indicating a significant relation between interhemispheric SSTs and the atmospheric response. These differences in the interhemispheric SST gradient have resulted in a global-scale shift of the intertropical convergence zone¹⁵ (Extended Data Fig. 1c,d), and, therefore, have affected the Sahel rainfall and VWS around the Atlantic basin³ (Fig. 1b,c) as well as the rainfall in other regions (Extended Data Fig. 1).

The differences in the SST gradient are systemic in the CMIP6 models, as almost all ensemble members predict that the trend for the SST gradient is higher than the observed trend (Fig. 1f). SST trends derived from the single-forcing runs in the Detection and Attribution Model Intercomparison Project (DAMIP; see 'Model data' in Methods) indicate that GHGs contribute to a positive interhemispheric SST gradient

(Fig. 1f and Extended Data Fig. 2). By contrast, the SST gradient for the NAT and AER runs are closely aligned with the observed values (Fig. 1f). We hypothesize that the disparity between trends for the ensemble mean of CMIP6 (CMIP6-EM) and observations may be attributed to at least two possible factors: (1) GHGs induce excess warming in the North Pacific and North Atlantic and insufficient warming in the Indian Ocean according to the models compared to observations ^{16,17} and (2) the simulated cooling in the Northern Hemisphere associated with aerosol emissions is underestimated, as there should be an interhemispheric gradient ¹⁸. A recent study suggested that these two factors may be interconnected ¹⁹. A thorough attribution of the cause for the model–data differences falls outside the scope of the present study and will be reported elsewhere.

A forced tropical AMCV since 1950

As the models misrepresent the post-1950 trend in the Atlantic climate, as shown in Fig. 1a–c, we linearly detrended all time series after 1950. (We return to the pre-1950 period later in the paper.) The results are shown in Fig. 2a–c. The thin and light-coloured time series are linearly detrended and normalized (to adjust for the erroneous signal-to-noise ratio; Table 1), and the bold and dark-coloured time series are additionally low-pass filtered by a 10 yr Butterworth filter to isolate the decadal variability. In contrast to Fig. 1a–c, a clear agreement between the modelled and observed AMV, VWS and Sahel rainfall emerges when the spurious long-term trend is appropriately removed.

The AMV was in a warm phase before the mid-1960s and again after the mid-1990s, but in between it was in a cold phase (Fig. 2a). The Sahel rainfall, NAH frequency and VWS covary with the AMV (Fig. 2b,c). During a warm AMV phase, precipitation over North Africa increases¹² (Fig. 3e,f), while NAHs become more frequent and intense¹ (Extended

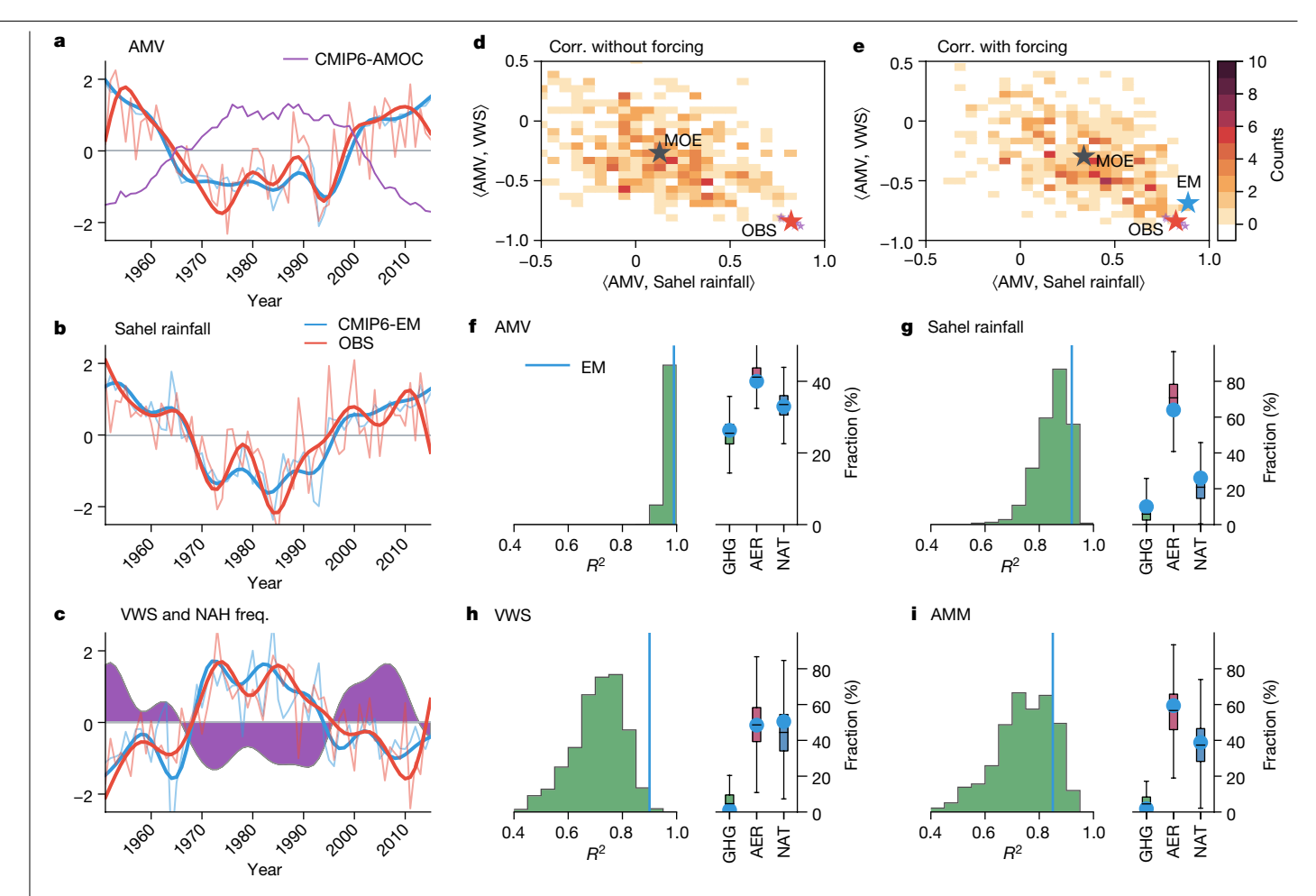


Fig. 2 | Forced post-1950 tropical AMCV. a-c, Simulated and observed JJASO indices from 1950 to 2014. The times series are normalized to the unit variance for comparison. The light, thin curves are detrended values, whereas the dark. bold curves have been low-pass filtered. AMV (a), Sahel rainfall (b), and VWS and observed Atlantic hurricane frequency (NAH freq.; shading; c) are shown. d, Two-dimensional histogram of correlations of the historical AMV with Sahel rainfall (x axis) and AMV with the VWS (y axis) in the model realizations with forced responses removed (Corr. without forcing; shading). The observed correlation (red star) is averaged across multi-source datasets. Correlations between different observations are plotted as small purple stars underneath the red star. The black star (MOE) is the mean of the shading, that is, for the

individual ensemble members. e, As in d but for correlations without forced responses being removed from the historical simulated data (Corr. with forcing). The light blue star (EM) is the correlation associated with the forced response. f, Distribution of R^2 by regressing the all-forcing AMV on single-forcing AMVs in a bootstrap (left), and the fraction of the total R^2 explained by GHGs, AER and NAT in the regression (right). The inner box runs from the first to the third quantile, whereas the whiskers denote the 10% and 90% percentiles. The light blue lines and dots were constructed using data from all members. **g**-**i**, As **f** but for Sahel rainfall (**g**), VWS (**h**) and AMM (**i**). See Methods for the definition of AMV, AMM, Sahel rainfall and VWS, and how the correlations and regressions were performed.

Data Fig. 3a-c). The hurricane genesis region (see 'Statistics of hurricane variability and genesis' in Methods) also shifts with the phase of AMV, with most hurricanes being generated in the MDR during a positive AMV, but the region shifts to the north and west to the Bermuda Sea during a negative AMV (Extended Data Fig. 3d-g), when the hurricane density and genesis is also suppressed. The shift is favoured by the shift in VWS²⁰.

Beyond the Atlantic, the forced Northern Hemisphere atmospheric teleconnections and rainfall associated with the AMV are consistent between CMIP6 simulations and observations (Fig. 3), which differs from what was found in previous studies^{21,22}. In the upper troposphere, a stationary circum-global teleconnection pattern persists at mid-latitudes in the Northern Hemisphere (Fig. 3a,b). At lower levels, there is anomalous low pressure in the Mediterranean region and Central Asia, while an anomalous subtropical high emerges in the North Pacific²² (Fig. 3c,d), both of which enhance the southerly flow and, therefore, rainfall in India, East Asia, Siberia and Alaska (Fig. 3e,f).

The consistency between the simulated forced responses and observations suggests that the recent tropical AMCV is driven by external forcings. We calculated the correlation between the simulated and observed AMV, Sahel rainfall and VWS. Correlations associated with the forced response (ensemble mean; see 'Definitions' in Methods) are high (over 0.9), higher than all but a very few of the individual model runs and far higher than the average of individual members (mean of the ensemble, MOE; see 'Definitions' in Methods) (Extended Data Fig. 4a-c). This result confirms that the observed variability is consistent with the response to forcing, but it does not rule out some influences from internal processes.

To test the alternative possibility that the AMCV is due to internal processes, we examined the correlations of AMV with Sahel rainfall and VWS in observations, in pre-industrial simulations (N = 3,100realizations) and in historical simulations after removing the forced responses from each ensemble member ($N \approx 400$, see 'Model data' and 'Quantifying the correlations between AMV/AMM and VWS and Sahel rainfall' in Methods). This allowed us to test whether the covariability that makes AMCV a single mode arises without the influence of forcing. Figure 2d and Extended Data Fig. 5a show that the absolute value of the correlation between the observed AMV and VWS

Table 1 | Modelled and observed variance and signal-to-noise ratio for the post-1950 AMV, VWS, Sahel rainfall and AMM

	Variance	ACI	AMV	vws	Sahel rainfall	AMM
CMIP6	MOE	All	0.0283	0.6794	0.0192	0.0175
		High	0.0243	0.8155	0.0324	0.0159
		Low	0.0340	0.5918	0.0146	0.0171
	EM	All	0.0141	0.0459	0.0031	0.0027
		High	0.0136	0.0597	0.0071	0.0031
		Low	0.0186	0.0450	0.0026	0.0033
	IV = MOE-EM	All	0.0142	0.6335	0.0160	0.0148
		High	0.0107	0.7558	0.0254	0.0128
		Low	0.0153	0.5468	0.0120	0.0138
	S/N ratio = EM/IV	All	1.00	0.07	0.20	0.19
		High	1.26	0.08	0.28	0.25
		Low	1.21	0.08	0.22	0.24
OBS	MOE	-	0.0302	2.2867	0.0685	0.0285
	EM	-	0.0250	1.9778	0.0618	0.0192
	IV = MOE-EM	_	0.0052	0.3089	0.0067	0.0093
	S/N ratio = EM/IV	_	4.82	6.40	9.26	2.05

All time series were detrended and low-pass filtered before the variance was calculated. See Methods for the definition of the ensemble mean (EM) and the MOE variance of the model data. The high and low aerosol–cloud interaction (ACI) models are shown in Extended Data Fig. 9. IV denotes the internal variability. For observations, the MOE variance is the total variance. The variance of the ensemble mean was calculated based on the square of the correlation with CMIP6-EM. Units for AMV, AMM, Sahel rainfall and VWS variances are $^{\circ}$ C², $^{\circ}$ C², mm²day² and m²s² respectively. S/N ratio, signal-to-noise ratio.

or Sahel rainfall is over 0.85. Figure 2d shows that none of the unforced model runs attained such high values, and that, when averaged over the ensemble (MOE; see 'Definitions' in Methods), the correlations are only approximately –0.2 and 0.3 (see also Extended Data Fig. 5a). That the modelled correlations have a large spread and relatively low MOEs is because the covariability between the AMV and its impacts may be interrupted or strengthened by other processes, such as El Niñosouthern oscillation²³ and the Pacific decadal oscillation²⁴. This suggests that internal dynamics produces some covariability in the tropical AMCV, but the very strong observed covariability is highly unlikely to be due to internal dynamics alone.

Using the historical runs (with both the forced response and internal variability included) shifts the cluster of correlations slightly toward higher values (compare Fig. 2e with Fig. 2d), though the MOE correlations in Fig. 2e are still much smaller than the observed correlation. By contrast, the correlations associated with the forced response alone (ensemble mean correlations) are close to the observed correlation (Fig. 2e, blue star). These results show that forcing somewhat improves the correlations of single realizations^{3,25}, but the observed high correlations are very unlikely to occur in the real world unless they are largely driven by external forcings with little influence from internal dynamics. This further implies that climate models have a low signal-to-noise ratio in the coupled AMCV because single realizations are dominated by internal variability (compare Fig. 2d with Fig. 2e, shading and black star), but they have a high signal-to-noise ratio in a single realization of the real world because it is mostly forced (Fig. 2e, blue and red star).

Tropical AMCV driven by AER and NAT

To diagnose the role of single forcings, we regressed the detrended and low-passed forced response in the all-forcing run onto the corresponding forced response in single-forcing runs for GHGs, AER and NAT. We used a bootstrap regression method to get uncertainty estimates for the regressions (see 'Quantifying the role of single forcings' in Methods). The multilinear regression successfully captured the variability of the forced AMCV, as indicated by the high R^2 values in the regression (Fig. 2f-h, left), especially for the all-member ensemble mean (blue lines in Fig. 2f-h). The fraction of R^2 explained by each forcing was quantified by a dominance analysis, which is a method for evaluating the role of predictors in a multilinear regression (Methods). The fractions are shown in Fig. 2f-h (right). For AMV, the contributions of GHGs. AER and NAT are similar in magnitude, but the role of GHGs is reduced in Sahel rainfall and VWS (Fig. 2f-h). VWS is driven by both AER and NAT, whereas AER is dominant for Sahel rainfall²⁶. The impact of individual forcings is also reflected in their regression coefficients. The distributions of regression coefficients for single forcings are similar for AMV, whereas the coefficients for GHGs for Sahel rainfall and VWS are close to zero (Extended Data Fig. 6).

Mechanism of the tropical impacts

We hypothesize that the tropical impacts of the AMV are associated with the dipole SST anomaly in the tropical Atlantic, which excites a Gill-type response⁸ to aerosol forcing. In the positive AMV, an anticyclonic anomaly persists in the tropical North Atlantic that extends to North Africa in the upper troposphere (Fig. 3a,b), whereas a cyclonic anomaly persists in the lower atmosphere (Fig. 3c,d). This local baroclinic mode is predicted by the Gill model with a dipole heating anomaly across the equator (fig. 2 in ref. 8). As a result, the southern edge of an anticyclone produces an easterly anomaly that reduces the VWS in the MDR and, thus, favours NAH activity. The southern flank of a cyclone induces a westerly trade wind anomaly that transports water vapour to the Sahel region producing rainfall (Fig. 3e,f).

This mechanism is confirmed by the tropical North and South Atlantic SST gradient (known as the Atlantic meridional mode or AMM; see 'Definitions' in Methods) in model simulations, which resembles the low-frequency AMM that strongly relates to hurricane activity²⁷. The forced AMM in the model is highly correlated with the observations, again indicating a strong influence from forcing (Extended Data Fig. 4d). The correlations between the modelled Sahel rainfall and VWS with AMM are higher than those with the modelled AMV (compare Extended Data Fig. 5c with Fig. 2e and Extended Data Fig. 5a with Extended Data Fig. 5b), especially for the forced response. The differences between the tropical North and South Atlantic SSTs largely remove the secular warming trend induced by GHG forcing (compare Fig. 1a with Fig. 4c). The absence of a secular trend in AMM is also true for Sahel rainfall and VWS over the past century (Fig. 4c), reinforcing the notion that AMM is a superior metric compared to AMV. In addition, a dominance analysis shows that GHGs, AER and NAT make similar relative contributions to AMM, Sahel rainfall and VWS. In particular, GHGs have a negligible role (Fig. 2i), because the warming due to GHGs is largely uniform in the tropics (Extended Data Fig. 7a). By contrast, heating by AER and NAT have spatial gradients (Extended Data Fig. 7b,c), which perturb the surface radiation and alters the SST^{3,7,28}.

This mechanism is also qualitatively supported by an idealized sensitivity experiment with a slab ocean model (SOM), in which an anomalous heat convergence is placed in the tropical North Atlantic (see 'Sensitivity experiment' in Methods). The surface heating enhances tropical rainfall and releases latent heat, which triggers an anticyclone at high levels in the atmosphere west of the basin, weakening the VWS²⁹ (Extended Data Fig. 8a). Together with the extratropical SST³⁰ and SST fingerprints caused by AER^{31,32}, the surface heating may also trigger circum-global atmospheric teleconnections through the tropical pathway³³, leading to an intensified Pacific subtropical high and rainfall in East Asia (Extended Data Fig. 8).

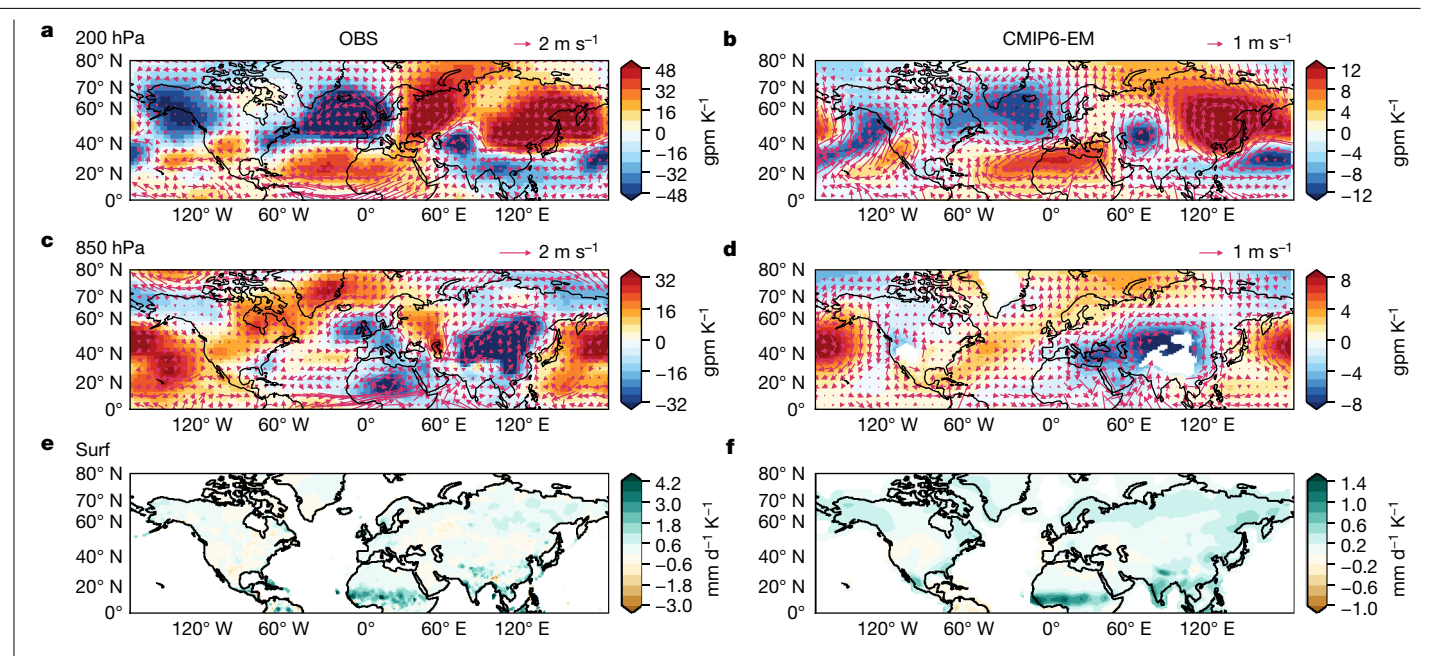


Fig. 3 | Simulated and observed climate change associated with AMV in the Northern Hemisphere. a, Regression of the JJASO 200 hPa geopotential height and circulation on the AMV index for observations (OBS). c, As a but for 850 hPa. e, As a but for rainfall. The regressions were calculated as the geopotential height or rainfall difference divided by the SST difference between AMV+ (pre-1965 and post-1995) and AMV- (1965-1995) to suppress the influence of

interannual variability. b,d,f, As a, c and e but for CMIP6-EM. Shown are 200 hPa geopotential height (b), 850 hPa geopotential height (d) and Rainfall (f). The regressions were performed in the regular way. The circulations in ${\bf b}$ and ${\bf d}$ were calculated based on the geostrophic balance. In $\mathbf{a} - \mathbf{d}$, the zonal mean geopotential height is removed. The maps were plotted using the cartopy package in Python.

Signal-to-noise paradox in the tropical AMCV

Although there is a strong temporal correlation between the simulated forced response and observed data (Extended Data Fig. 4), the variance of the modelled forced response (ensemble mean variance) is much smaller than that of the observations, which is estimated based on the correlation between the model ensemble mean and observations (Extended Data Fig. 9a-d and Table 1). This is a consequence of what is referred to as the signal-to-noise paradox¹⁰. It has also been documented for the North Atlantic oscillation 9,11. One possible cause of the small ensemble mean variance is the weak indirect-aerosol effects in some models. A supporting example is that CMIP3 and CMIP5 models without indirect-aerosol effects exhibit smaller variances compared to those that include them^{3,7}. However, in a comparison of CMIP6 models with high and low aerosol-cloud interactions, there is little difference in the signal-to-noise ratio (Extended Data Fig. 9e-l and Table 1). By contrast, a SOM produces a high ensemble mean and MOE variance, even higher than that observed, suggesting that the damping by ocean processes may be too strong in fully coupled models³⁴. Recent work has also suggested that increasing model resolution may ameliorate signal-to-noise errors³⁵. The EC-Earth3 model has the highest resolution and produces a more accurate interhemispheric SST gradient and covariability in AMCV.

Pre-1950 tropical AMCV

We now return to the AMCV before 1950. Figure 4d-g, the normalized pre-1950 time series (without detrending), shows that forcing has a discernible influence, even in this earlier period. This is surprising in view of the relatively weaker climate forcing in the pre-1950 era. Namely, there was a much lower signal-to-noise ratio in the models than from 1950 on (Extended Data Table 1a).

However, observed correlations between North Atlantic SST/AMM and the tropical impacts are more consistent with the average of correlations from individual simulations (MOE) than with the forced response (ensemble mean), marked as OBS and MOE in Fig. 4a,b. This suggests that when the external forcing is weaker in the early period, the tight coupling found in post-1950 AMCV is not present, implying that the pre-1950 AMCV is substantially influenced by internal variability. The total change in the variance in the observed AMCV also substantiates less of a role for forcing in the pre-1950 tropical AMCV. There is an increase in post-1950 AMCV variance when anthropogenic forcing increases (Extended Data Table 1b). Assuming that the observed variance due to internal variability remains roughly constant, then the forced variance in the earlier period is lower compared to the later period (Extended Data Table 1b), consistent with the fact that the anthropogenic components of the forcing are weaker.

Also, note that both observations^{36,37} and climate forcings³⁸ in the early 20th century have more uncertainty. The observed pre-1950 correlations between AMM and tropical impacts vary from 0.1 to 0.6 depending on the dataset used (Fig. 4b, small purple stars), whereas the spread of post-1950 correlations is negligible (Fig. 2e and Extended Data Fig. 5). The low signal-to-noise ratio in the modelled pre-1950 AMCV (Extended Data Table 1a) calls into question whether our approximately 400-member ensemble is large enough to extract the forced signal amidst the noise in the early period, albeit that some AMCV components show a forced response. These data uncertainties preclude a definitive attribution for the pre-1950 AMCV.

Discussion and summary

Simulations with constant external forcings (for example, pre-industrial control runs) show covariability between AMV and Sahel rainfall or hurricane activity (NAH)^{4,39,40}, which leads to the conclusion that tropical aspects of AMCV are a feature of internal oceanic and atmospheric dynamics^{5,6,41}. As we have seen, however, the simulated covariability, measured as the correlations between AMV and its impacts, is much weaker than the observed values, which have been above 0.8 since World War ${\rm II^{4,39,40}}.$ The linkage between the Atlantic meridional overturning circulation (AMOC) or the North Atlantic oscillation and AMCV

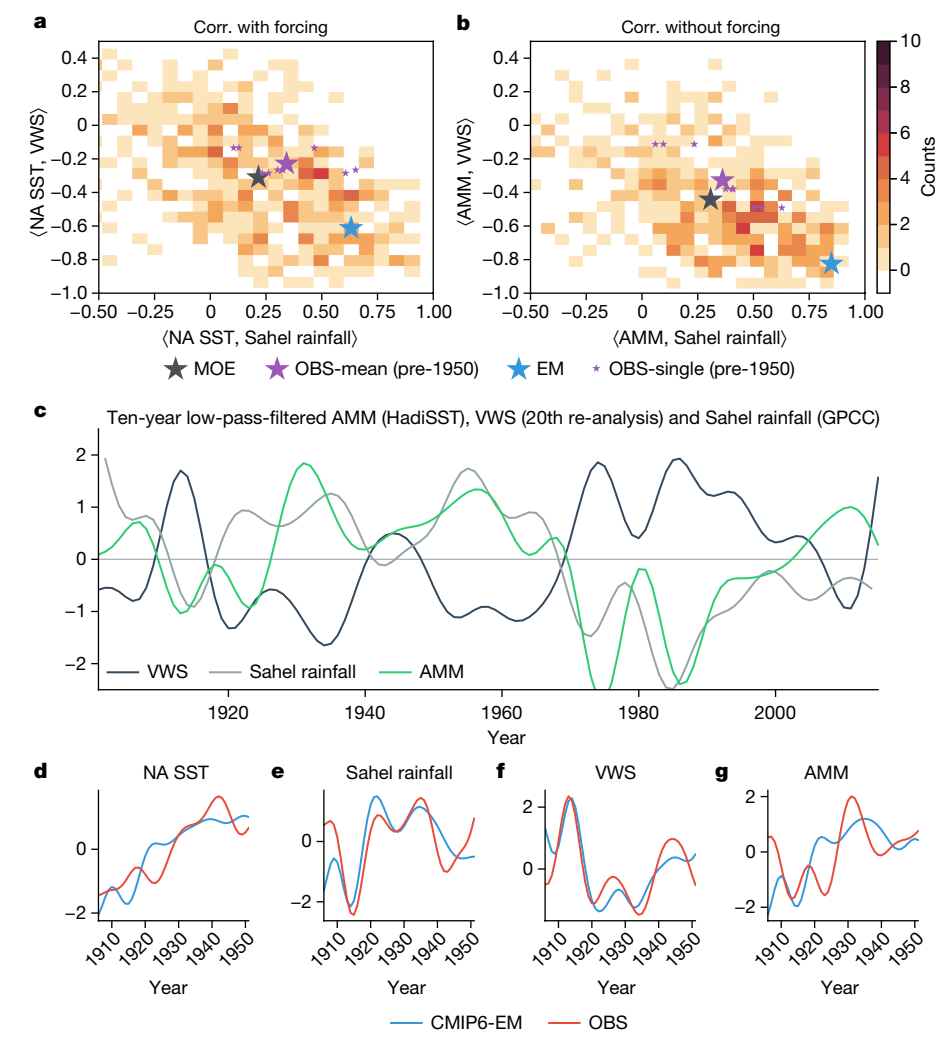


Fig. 4 | **Pre-1950 tropical AMCV. a**, Two-dimensional histogram of correlations between low-pass-filtered North Atlantic (NA) SST and Sahel rainfall (x axis) and VWS (y axis) in model realizations (shading) and observations (OBS; big purple star) in 1905–1950. The small purple stars are correlations between different observation datasets. The blue star is the ensemble mean (EM). The

black star is the MOE. **b**, As **a** but for correlations between AMM and tropical impacts. **c**, Observations of normalized AMM, VWS and Sahel rainfall from 1900 to 2014. **d**, Low-pass-filtered North Atlantic SST, 1905–1950. **e**–**g**, As in **d** but for Sahel rainfall (**e**), VWS (**f**) and AMM (**g**). In **c**–**g**, the time series are not detrended.

is observed in pre-industrial control runs, but it varies significantly across models 42,43 and can even have the opposite sign in historical simulations 44,45 . Figure 2a shows that although the simulated forced AMOC is associated with the forced AMV, they are anti-correlated, which is contrary to what one would expect if the internal fluctuations in AMOC were the driver 5 .

Past work has shown that historical simulations forced by realistic radiative forcings exhibit spatial discrepancies with observations of SSTs and rainfall patterns²², although there has been some improvement in the temporal covariability of the tropical AMCV components^{3,25,28,46,47}. Consistent with our results, anthropogenic (AER) and natural (NAT) aerosols have been suggested as a driver of the AMCV^{7,34,48,49}, although some have questioned whether the aerosol forcing is too large^{5,50}.

Here we have shown that a systemic interhemispheric SST difference between CMIP6 models and observations that develops after 1950 induces a spurious trend in the tropical Atlantic (Fig. 1). When we remove this trend, we find that the tropical AMCV is largely driven by anthropogenic and volcanic aerosol forcings in the post-1950 period (Fig. 2), especially for Atlantic hurricanes, which are often thought to be internally driven 4.20.24. Further, we provide a physical link from this

north—south Atlantic SST difference to the change in Sahel rainfall and wind shear in the MDR, a determinant of hurricane activity. The tropical AMCV in the early 20th century appears to be more affected by internal variability than in the later period when anthropogenic forcing is strong (Fig. 4a,b). Even so, the forced response is evident in tropical impacts in multidecadal periods (Fig. 4d–g). Our results demonstrate the predictive potential of the tropical AMCV, which is underestimated in state-of-the-art climate models due to the signal-to-noise paradox. Rectifying this signal-to-noise error in climate models could unlock this potential, improving our ability to predict and adapt to a rapidly changing climate. Our findings also emphasize that large ensemble simulations can serve as a viable approach for predicting the near-future AMCV, as has been demonstrated for the North Atlantic oscillation $^{9.11}$.

Online content

Any methods, additional references, Nature Portfolio reporting summaries, source data, extended data, supplementary information, acknowledgements, peer review information; details of author contributions and competing interests; and statements of data and code availability are available at https://doi.org/10.1038/s41586-023-06489-4.

- Goldenberg, S. B., Landsea, C. W., Mestas-Nuñez, A. M. & Gray, W. M. The recent increase in Atlantic hurricane activity: causes and implications. Science 293, 474-479 (2001).
- 2. Gray, W. M. Strong association between West African rainfall and U.S. landfall of intense hurricanes. Science 249, 1251-1256 (1990).
- Dunstone, N. J., Smith, D. M., Booth, B. B. B., Hermanson, L. & Eade, R. Anthropogenic aerosol forcing of Atlantic tropical storms. Nat. Geosci. 6, 534-539 (2013).
- Yan, X., Zhang, R. & Knutson, T. R. The role of Atlantic overturning circulation in the recent decline of Atlantic major hurricane frequency. Nat. Commun. 8, 1695 (2017).
- Zhang, R. et al. A review of the role of the Atlantic meridional overturning circulation 5. in Atlantic multidecadal variability and associated climate impacts. Rev. Geophys. 57, 316-375 (2019).
- Clement, A. et al. The Atlantic multidecadal oscillation without a role for ocean 6 circulation. Science 350, 320-324 (2015).
- 7. Booth, B. B., Dunstone, N. J., Halloran, P. R., Andrews, T. & Bellouin, N. Aerosols implicated as a prime driver of twentieth-century North Atlantic climate variability. Nature 484. 228-232 (2012).
- 8. Gill, A. F. Some simple solutions for heat-induced tropical circulation, Q. J. R. Meteorol. Soc. 106, 447-462 (1980).
- 9. Smith, D. M. et al. North Atlantic climate far more predictable than models imply. Nature 583, 796-800 (2020).
- 10 Scaife, A. A. & Smith, D. A signal-to-noise paradox in climate science, npi Clim. Atmos. Sci. 1, 28 (2018).
- 11 Klavans, J. M., Cane, M.A., Clement, A. C. & Murphy, L. N. NAO predictability from external forcing in the late 20th century. npj Clim. Atmos. Sci. 4, 22 (2021).
- Folland, C. K., Palmer, T. N. & Parker, D. E. Sahel rainfall and worldwide sea temperatures, 12. 1901-85. Nature 320, 602-607 (1986).
- Sutton, R. T. & Hodson, D. L. Atlantic Ocean forcing of North American and European 13. summer climate. Science 309, 115-118 (2005).
- Chiang, J. C. H. & Friedman, A. R. Extratropical cooling, interhemispheric thermal gradients, and tropical climate change. Annu. Rev. Earth Planet. Sci. 40, 383-412 (2012).
- Kang, S. M., Held, I. M., Frierson, D. M. W. & Zhao, M. The response of the ITCZ to extratropical thermal forcing: idealized slab-ocean experiments with a GCM. J. Clim. 21,
- Hu, S. & Fedorov, A. V. Indian Ocean warming can strengthen the Atlantic meridional overturning circulation. Nat. Clim. Change 9, 747-751 (2019).
- 17. Wills, R. C. J., Dong, Y., Proistosecu, C., Armour, K. C. & Battisti, D. S. Systematic climate model biases in the large-scale patterns of recent sea-surface temperature and sea-level pressure change. Geophys. Res. Lett. 49, e2022GL100011 (2022).
- Deser, C. et al. Isolating the evolving contributions of anthropogenic aerosols and greenhouse gases: a new CESM1 Large Ensemble Community resource, J. Clim. 33. 7835-7858 (2020).
- Wang, C., Soden, B. J., Yang, W. & Vecchi, G. A. Compensation between cloud feedback 19. and aerosol-cloud interaction in CMIP6 models, Geophys, Res. Lett. 48, e2020GL091024
- Ting, M., Kossin, J. P., Camargo, S. J. & Li, C. Past and future hurricane intensity change along the U.S. East Coast. Sci. Rep. 9, 7795 (2019).
- Ting, M., Kushnir, Y. & Li, C. North Atlantic multidecadal SST oscillation: external forcing versus internal variability. J. Mar. Syst. 133, 27-38 (2014).
- Si, D., Hu, A., Jiang, D. & Lang, X. Atmospheric teleconnection associated with the Atlantic multidecadal variability in summer: assessment of the CESM1 model. Clim. Dyn. 60, 1043-1060 (2023).
- Pielke, R. A. Jr & Landsea, C. N. La Niña, El Niño, and Atlantic hurricane damages in the United States. Bull. Am. Meteorol. Soc. 80, 2027-2034 (1999).
- 24. Li, W., Li, L. & Deng, Y. Impact of the interdecadal Pacific oscillation on tropical cyclone activity in the North Atlantic and eastern North Pacific. Sci. Rep. 5, 12358 (2015).
- Smith, D. M. et al. Skilful multi-year predictions of Atlantic hurricane frequency. Nat. Geosci, 3, 846-849 (2010).
- 26. Ackerley, D. et al. Sensitivity of twentieth-century Sahel rainfall to sulfate aerosol and CO₂ forcing. J. Clim. 24, 4999-5014 (2011).
- Vimont, D. J. & Kossin, J. P. The Atlantic meridional mode and hurricane activity. Geophys. Res. Lett. https://doi.org/10.1029/2007GL029683 (2007).
- Zhang, S., Stier, P., Dagan, G. & Wang, M. Anthropogenic aerosols modulated 20th-century Sahel rainfall variability via their impacts on North Atlantic sea surface temperature, Geophys, Res. Lett. 49, e2021GL095629 (2022).

- Sutton, R. T. & Hodson, D. L. R. Climate response to basin-scale warming and cooling of the North Atlantic Ocean. J. Clim. 20, 891-907 (2007).
- 30. Dunstone, N. J., Smith, D. M. & Eade, R. Multi-year predictability of the tropical Atlantic atmosphere driven by the high latitude North Atlantic Ocean. Geophys. Res. Lett. https://doi.org/10.1029/2011GL047949 (2011).
- Bollasina, M. A., Ming, Y. & Ramaswamy, V. Anthropogenic aerosols and the weakening of the South Asian summer monsoon. Science 334, 502-505 (2011).
- Qin, M., Dai, A. & Hua, W. Aerosol-forced multidecadal variations across all ocean basins in models and observations since 1920. Sci. Adv. 6, eabb0425 (2020).
- Ruprich-Robert, Y. et al. Assessing the climate impacts of the observed Atlantic multidecadal variability using the GFDL CM2. 1 and NCAR CESM1 global coupled models. J. Clim. **30**, 2785–2810 (2017).
- Murphy, L. N., Klavans, J. M., Clement, A. C. & Cane, M. A. Investigating the roles of external forcing and ocean circulation on the Atlantic multidecadal SST variability in a large ensemble climate model hierarchy. J. Clim. 34, 4835-4849 (2021).
- Scaife, A. A. et al. Does increased atmospheric resolution improve seasonal climate predictions, Atmos. Sci. Lett. 20, e922 (2019).
- Chan, D., Kent, E. C., Berry, D. I. & Huybers, P. Correcting datasets leads to more 36. homogeneous early-twentieth-century sea surface warming. Nature 571, 393-397 (2019).
- 37 Berntell, E., Zhang, Q., Chafik, L. & Körnich, H. Representation of multidecadal Sahel rainfall variability in 20th century reanalyses. Sci. Rep. 8, 10937 (2018).
- 38 Fyfe, J. C., Kharin, V. V., Santer, B. D., Cole, J. N. S. & Gillett, N. P. Significant impact of forcing uncertainty in a large ensemble of climate model simulations. Proc. Natl Acad. Sci. USA 118, e2016549118 (2021).
- Knight, J. R., Folland, C. K. & Scaife, A. A. Climate impacts of the Atlantic multidecadal 39. oscillation. Geophys. Res. Lett. https://doi.org/10.1029/2006GL026242 (2006).
- Martin, E. R., Thorncroft, C. & Booth, B. B. B. The multidecadal Atlantic SST—Sahel rainfall teleconnection in CMIP5 simulations. J. Clim. 27, 784-806 (2014).
- Wills, R. C. J., Armour, K. C., Battisti, D. S. & Hartmann, D. L. Ocean-atmosphere dynamical coupling fundamental to the Atlantic multidecadal oscillation. J. Clim. 32, 251-272 (2019)
- Ba, J. et al. A multi-model comparison of Atlantic multidecadal variability. Clim. Dyn. 43, 2333-2348 (2014).
- Yan, X., Zhang, R. & Knutson, T. R. Underestimated AMOC variability and implications for AMV and predictability in CMIP models. Geophys. Res. Lett. 45, 4319-4328 (2018).
- 44. Zhang, L. & Wang, C. Multidecadal North Atlantic sea surface temperature and Atlantic meridional overturning circulation variability in CMIP5 historical simulations. J. Geophys. Res. Oceans 118, 5772-5791 (2013).
- Klavans, J. M., Clement, A. C. & Cane, M. A. Variable external forcing obscures the weak relationship between the NAO and North Atlantic multidecadal SST variability. J. Clim. 32. 3847-3864 (2019).
- Giannini, A. & Kaplan, A. The role of aerosols and greenhouse gases in Sahel drought and 46. recovery, Clim. Change 152, 449-466 (2019).
- Herman, R. J., Giannini, A., Biasutti, M. & Kushnir, Y. The effects of anthropogenic and volcanic aerosols and greenhouse gases on twentieth century Sahel precipitation. Sci. Rep. 10, 12203 (2020).
- Klavans, J. M., Clement, A. C., Cane, M. A., & Murphy, L. N. The evolving role of external forcing in North Atlantic SST variability over the last millennium. J. Clim. 35, 2741–2754 (2022).
- 49. Watanabe, M. & Tatebe, H. Reconciling roles of sulphate aerosol forcing and internal variability in Atlantic multidecadal climate changes. Clim. Dyn. 53, 4651-4665 (2019).
- Zhang, R. et al. Have aerosols caused the observed Atlantic multidecadal variability. J. Atmos. Sci. 70, 1135-1144 (2013).

Publisher's note Springer Nature remains neutral with regard to jurisdictional claims in published maps and institutional affiliations.

Springer Nature or its licensor (e.g., a society or other partner) holds exclusive rights to this article under a publishing agreement with the author(s) or other rightsholder(s); author self-archiving of the accepted manuscript version of this article is solely governed by the terms of such publishing agreement and applicable law.

© The Author(s), under exclusive licence to Springer Nature Limited 2023

Methods

Definitions

As we are mostly focussed on AMV-related impacts, including NAH and Sahel rainfall, the current study uses mean annual time series for JJASO from CMIP6 and observations. The AMV is defined as the linearly detrended, area-averaged, and 10 yr low-passed (Butterworth filter) SST anomalies over the North Atlantic 51 (0°-60° N, 70° W-0°).

Sahel rainfall is precipitation over North Africa $(10-20^{\circ} \text{ N}, 20^{\circ} \text{ W}-40^{\circ} \text{ E})$. The VWS is the difference between the zonal wind at 200 and 850 hPa over the MDR $(80-20^{\circ} \text{ W}, 10-20^{\circ} \text{ N})$. To analyse their multidecadal variability, both Sahel rainfall and VWS were linearly detrended and 10 yr low-pass-filtered, except in Figs. 1 and 4.

The hemispheric SST gradient was calculated as the difference in the SSTs between the Northern Hemisphere ($30-60^\circ$ N) and the Southern Hemisphere (40° S -0°), as significant model–data SST discrepancy exists

We use the tropical Atlantic SST gradient (AMM) as an alternative to the AMV index. The AMM is here taken as the difference between the tropical North Atlantic (0° – 35° N) and the South Atlantic (35° S -0°). The AMM naturally filters out the global warming trend over the past century, like the non-detrended VWS and Sahel rainfall in the past century (Fig. 4c).

In the model, the forced response is calculated as the ensemble mean:

$$EM = \frac{1}{N} \sum_{i=1}^{N} f_i,$$

in which N is the number of ensemble members and f_i is the realization of member i.

For the forced response of all indices, we first calculate the ensemble mean and then do low-pass filtering and detrending. As the ensembles are large and the internal variations of individual members are, on average, uncorrelated in time, the ensemble mean is an excellent approximation of only the forced response³⁴. Thus, the ensemble mean correlation with observations is a good measure of the correlation between the forced response and observations. For example, the ensemble mean correlation with the observed AMV:

$$\langle AMV_{EM}, AMV_{OBS} \rangle = \left\langle \frac{1}{N} \sum_{i=1}^{N} AMV_{i}, AMV_{OBS} \right\rangle$$

where $\langle x, y \rangle$ denotes the Pearson correlation between x and y.

By contrast, the MOE includes both forced and internal responses. To calculate the MOE correlation with observation, we first calculate the correlation between the low-pass-filtered and detrended realization f_i with the low-pass-filtered and detrended observations and then average these correlations over all members:

$$\langle AMV_{MOE}, AMV_{OBS} \rangle = \frac{1}{N} \sum_{i=1}^{N} \langle AMV_i, AMV_{OBS} \rangle$$

We also measured the correlation between AMV/AMM and their tropical impacts on the observations and models. For example, the ensemble mean correlation in the modelled AMV and VWS is due to a forced response:

$$\langle AMV, VWS \rangle_{EM} = \left\langle \frac{1}{N} \sum_{i=1}^{N} AMV_i, \frac{1}{N} \sum_{i=1}^{N} VWS_i \right\rangle$$

whereas the MOE correlation in the modelled AMV and VWS is

$$\langle AMV, VWS \rangle_{MOE} = \frac{1}{N} \sum_{i=1}^{N} \langle AMV_i, VWS_i \rangle$$

We also calculated the variance of the ensemble mean and the MOE variance of all indices. The ensemble mean variance of AMV is

$$Var(AMV_{EM}) = Var\left(\frac{1}{N}\sum_{i=1}^{N}AMV_{i}\right)$$

whereas the MOE variance is

$$Var(AMV_{MOE}) = \frac{1}{N} \sum_{i=1}^{N} Var(AMV_i)$$

where Var(x) denotes the variance of x.

Observations

Several observation products were used in the present study to verify the robustness of our statistics. The AMV and AMM were calculated from the Extended Reconstructed Sea Surface Temperature version 5 dataset (ERSSTv5) from the National Oceanic and Atmospheric Administration (NOAA)⁵², Centennial in situ Observation-Based Estimates (COBE) SST2 data⁵³ and the Hadley Centre Sea Ice and SST dataset version 1.1 (HadISST)⁵⁴.

The Sahel rainfall was calculated from data from the Precipitation v. 4.05 dataset from the Climatic Research Unit (ref. 55) and data from the Global Precipitation Climatology Centre $(GPCC)^{56}$ and the University of Delaware 57 .

The VWS was calculated from a reanalysis by the National Centers for Environmental Prediction and the National Center for Atmospheric Research (NCEP-NCAR Reanalysis 1)⁵⁸ and the NOAA 20th Century Reanalysis⁵⁹.

The observed time series are very close from 1950, as identified by the correlation between AMV and its impacts in Fig. 2d,e (purple stars). However, the uncertainty increases in the pre-1950 period, when the correlations have a large spread (Fig. 4a,b, purple stars).

Model data

Model SSTs, geopotential heights and zonal wind data were taken from the CMIP6 archive: https://esgf-node.llnl.gov/projects/cmip6/. The forced response as the ensemble mean was then calculated by averaging approximately 400 ensemble members from the 46 models (Supplementary Table 1). However, as most models do not provide the field of AMOC, the AMOC index was calculated from 105 members in 24 models. The AMOC index is consistent with those in other studies 60,61. We also used a subset of the AMV for the 24 models that has a AMOC output, and the results are qualitatively consistent. To quantify the internal variability, the first member (r1i1p1f1) of the pre-industrial control runs was also downloaded from 31 models. We also obtained these variables from DAMIP (https://damip.lbl.gov) to quantify the role of GHGs (hist GHG), AER (hist aer) and NAT (hist nat).

Statistics of hurricane variability and genesis

Hurricane frequencies were calculated as in ref. 4 using the Hurricane Database (HURDAT).

Hurricane track density and genesis density were calculated for category "HU" in the Atlantic hurricane database (HURDAT2) from 1950 to 2014. We first counted the numbers of hurricanes in every grid (resolution: latitude $3^{\circ} \times \text{longitude } 7^{\circ}$) that hurricanes passed through in 1950–2014. We then normalized the numbers of hurricanes in each grid by dividing by the length of the AMV \pm phase to get the hurricane track density. According to Fig. 2, we defined the period before 1965 and after 1995 as AMV \pm , and the period in between as AMV \pm . The genesis density was calculated in the same way, but we counted only the first data point as the genesis location. To quantify the shift of genesis location in different AMV phases, we calculated the ratios of hurricanes generated in the MDR (10–20° N, 80–20° W) and over the Bermuda Sea (24–32° N, 90–60° W) to the total NAHs every year. The difference between these two ratios is plotted in Extended Data Fig. 3g (green curve).

Quantifying the correlations between AMV/AMM and VWS and Sahel rainfall

We quantified the correlations between AMV/AMM and VWS and Sahel rainfall associated with internal variability in two ways. First, we removed the forced response from ensemble members in the historical runs (1950–2014, $N \approx 400$) and then calculated the correlation between these variables (Fig. 2d). Second, we used data from 31 pre-industrial control runs with fixed forcings, discarding the first 100 yr to remove spin-up effects. Then we randomly picked up a continuous 65 yr time series from the run (equal to the length of the historical run in 1950–2014) and calculated AMV, AMM, VWS and Sahel rainfall based on the aforementioned definitions. This process was repeated 100 times for each run, so in total we have 3,100 (31 × 100) realizations. The correlation distributions from the two methods looks similar (compare Extended Data Fig. 5a with Fig. 2d and Extended Data Fig. 5b with Extended Data Fig. 5c).

We also quantified the correlations between AMV/AMM and VWS and Sahel rainfall in historical runs (1950–2014, $N \approx$ 400, with the forced response not removed) in the same way. Including forcings into single realizations indeed shifts the correlation distribution toward a higher value (Fig. 2d,e). Finally, the correlations associated with the forced response were calculated from the ensemble mean for AMV, AMM, VWS and Sahel rainfall.

The pre-1950 correlations between AMV/AMM and VWS and Sahel rainfall for the simulations were calculated in the same way but without detrending the observational or model data (Fig. 4a,b). The results after detrending pre-1950 were quantitatively unchanged (not shown).

As we have multiple observational datasets, a set of correlations, say between AMV and VWS, was calculated for each combination (N=6, for three SST datasets times two VWS datasets). For Sahel rainfall, N=9 (3 × 3). The observed correlations from 1950 are insensitive to the data product used, as the spread of correlations was small (standard deviation <0.03) from 1950 (Fig. 2d,e). Before 1950, we have only the 20th Reanalysis data for calculating the VWS, so correlations related to VWS have only three samples.

Quantifying the role of single forcings

To investigate the role of single forcings in the AMCV, we assumed that the forced responses of AMV/AMM, VWS and Sahel rainfall in CMIP6 are a linear combination of those in the single-forcing runs from DAMIP. Thus, we regressed the all-forcing AMV/AMM, VWS and Sahel rainfall data onto those from single-forcing runs. As we have hundreds of model realizations, we performed the regression with a bootstrap method. First, we randomly selected 70 (150) members with duplication from single-forcing runs (all-forcing historical runs) and calculated the ensemble mean, detrended the data and calculated a 7 yr running mean for the AMV/AMM and their impacts. Second, we performed a dominance analysis 62 , which is a method for quantifying the total R^2 in a multilinear regression explained by each predictor: GHGs, AER and NAT. This process was repeated 1,000 times. Finally, we performed the dominance analysis for the all-member ensemble mean without duplication ($N \approx 400$ for the all-forcing run, N varies for single-forcing runs, see Supplementary Table 1). The results are presented as light blue lines and dots in Fig. 2f-i. We also performed a relative weight analysis 63 of the same dataset, which is another way of quantifying the role of a predictor in a multilinear regression. The results are highly similar to those from the dominance analysis.

Sensitivity experiment

An idealized sensitivity experiment was performed with Community Earth System Model 1.1 from NCAR (CESM1.1, ref. 64) in a SOM configuration with an atmospheric resolution of $0.9^{\circ} \times 1.25^{\circ}$ and an oceanic resolution of $1.125^{\circ} \times 0.27-0.54^{\circ}$ (f09_gx1v6). The configuration of the SOM consists of dynamic-thermodynamic atmosphere, land and sea

ice models. The ocean component was replaced with a SOM with only thermal coupling to the overlying atmosphere and sea ice. Surface heat flux, $Q_{\rm flx'}$ derived from model years 402 to 1510 of a long pre-industrial, control and fully coupled simulation, was used for dynamical ocean heat transport in SOM. In the sensitivity run, we added a uniform 10 W m⁻² to $Q_{\rm flx}$ over the tropical North Atlantic (0–30° N from Africa to the Americas) to intensify the AMM, as in the positive AMV. Both sensitivity and pre-industrial control runs were integrated for 100 years and the first 40 years were neglected because of model drift and spin-up. The response of the intensified AMM was calculated as the difference between the sensitivity and the pre-industrial control runs.

Data availability

Observed SST, rainfall and wind data were obtained from: ERSSTv5, https://psl.noaa.gov/data/gridded/data.noaa.ersst.v5.html; COBE SST2, https://psl.noaa.gov/data/gridded/data.cobe2.html; HadISST, https://www.metoffice.gov.uk/hadobs/hadisst/; Climatic Research Unit precipitation data, https://crudata.uea.ac.uk/cru/data/hrg/; GPCC precipitation data, https://psl.noaa.gov/data/gridded/data.gpcc.html; University of Delaware precipitation data, http://climate.geog.udel.edu/-climate/html_pages/download.html; NCEP-NCAR Reanalysis 1 data, https://psl.noaa.gov/data/gridded/data.ncep.reanalysis.html; and NOAA 20th Century Reanalysis data, https://psl.noaa.gov/data/gridded/data.20thC_ReanV3.html. Hurricane frequency data were obtained from HURDAT: HURDAT2, https://www.nhc.noaa.gov/data/; and HURDAT, https://www.aoml.noaa.gov/hrd/hurdat/comparison_table.html. All model data were taken from the CMIP6 and DAMIP archives: https://esgf-node.llnl.gov/projects/cmip6/ and https://damip.lbl.gov.

Code availability

The code for the dominance analysis can be found at: https://github.com/dominance-analysis/dominance-analysis. Other scripts to reproduce the results can be found at: https://doi.org/10.5281/zenodo.8098355.

- Enfield, D. B., Mestas-Nuñez, A. M. & Trimble, P. J. The Atlantic multidecadal oscillation and its relation to rainfall and river flows in the continental U.S. Geophys. Res. Lett. https:// doi.org/10.1029/2000GL012745 (2001).
- Huang, B. et al. Extended Reconstructed Sea Surface Temperature, version 5 (ERSSTv5): upgrades, validations, and intercomparisons. J. Clim. 30, 8179–8205 (2017).
- Hirahara, S., Ishii, M. & Fukuda, Y. Centennial-scale sea surface temperature analysis and its uncertainty. J. Clim. 27, 57–75 (2014).
- Rayner, N. A. et al. Global analyses of sea surface temperature, sea ice, and night marine air temperature since the late nineteenth century. J. Geophys. Res. Atmos. https://doi.org/ 10.1029/2002JD002670 (2003).
- Harris, I., Osborn, T. J., Jones, P. & Lister, D. Version 4 of the CRU TS monthly high-resolution gridded multivariate climate dataset. Sci. Data 7, 109 (2020).
- Becker, A. et al. A description of the global land-surface precipitation data products
 of the Global Precipitation Climatology Centre with sample applications including
 centennial (trend) analysis from 1901–present. Earth Syst. Sci. Data 5, 71–99 (2013).
- Willmott, C. J. & Matsuura, K. Smart interpolation of annually averaged air temperature in the United States. J. Appl. Meteorol. Climatol. 34, 2577–2586 (1995).
- Kalnay, E. et al. The NCEP/NCAR 40-year reanalysis project. Bull. Am. Meteorol. Soc. 77, 437–471 (1996).
- Slivinski, L. C. et al. Towards a more reliable historical reanalysis: improvements for version 3 of the Twentieth Century Reanalysis system. Q. J. R. Meteorol. Soc. 145, 2876–2908 (2019).
- Hassan, T., Allen, R. J., Liu, W. & Randles, C. A. Anthropogenic aerosol forcing of the Atlantic meridional overturning circulation and the associated mechanisms in CMIP6 models. Atmos. Chem. Phys. 21, 5821–5846 (2021).
- Menary, M. B. et al. Aerosol-forced AMOC changes in CMIP6 historical simulations Geophys. Res. Lett. 47, e2020GL088166 (2020).
- 62. Budescu, D. V. Dominance analysis: a new approach to the problem of relative importance of predictors in multiple regression. *Psychol. Bull.* **114**, 542–551 (1993).
- Johnson, J. W. A heuristic method for estimating the relative weight of predictor variables in multiple regression. Multivar. Behav. Res. 35, 1–19 (2000).
- Hurrell, J. W. et al. The Community Earth System model: a framework for collaborative research. Bull. Am. Meteorol. Soc. 94, 1339–1360 (2013).

Acknowledgements We acknowledge support for this work from the NOAA (Grant No. NA2OOAR4310400), the Climate and Large-Scale Dynamics programme of the National Science Foundation (Grant Nos. AGS 1735245 and AGS 1650209) and the Paleo Perspectives

on Climate Change programme of the National Science Foundation (Grant No. AGS 1703076). We also acknowledge high-performance computing support from Cheyenne (https://doi.org/10.5065/D6RX99HX) carried on NCAR's Computational and Information Systems Laboratory. We acknowledge climate modelling groups for producing model outputs and the Program for Climate Model Diagnosis and Intercomparison for maintaining the CMIP6 data archive.

Author contributions C.H. and A.C.C. conceived this study. C.H. performed the analysis and wrote the paper. S.M.K. supported the analysis. C.H., A.C.C., S.M.K., M.A.C., J.M.K., L.N.M. and T.M.F. discussed the results and contributed to the manuscript.

 $\textbf{Competing interests} \ \text{The authors declare no competing interests}.$

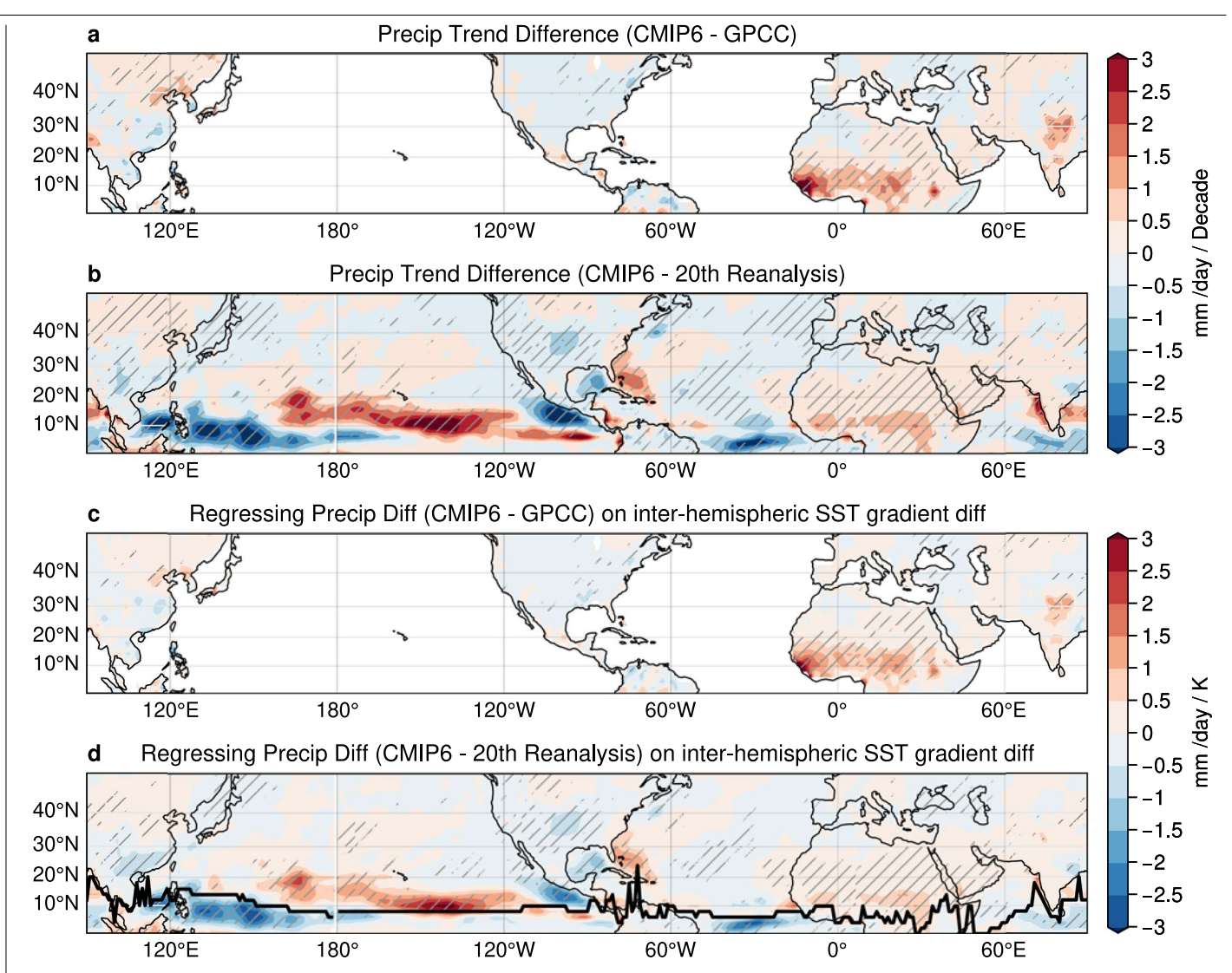
Additional information

Supplementary information The online version contains supplementary material available at https://doi.org/10.1038/s41586-023-06489-4.

Correspondence and requests for materials should be addressed to Chengfei He.

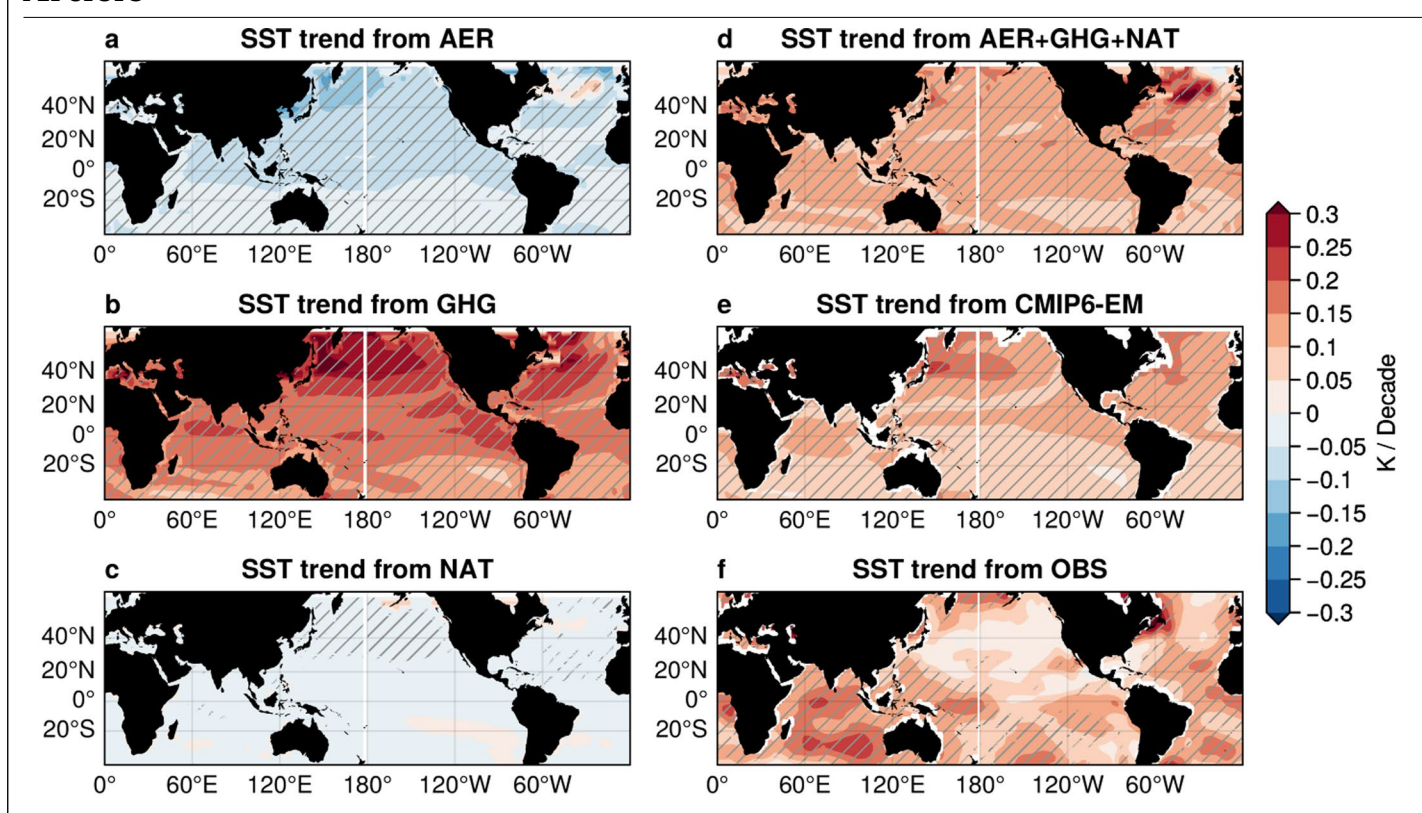
Peer review information Nature thanks Ben Booth and the other, anonymous, reviewer(s) for their contribution to the peer review of this work.

Reprints and permissions information is available at http://www.nature.com/reprints.



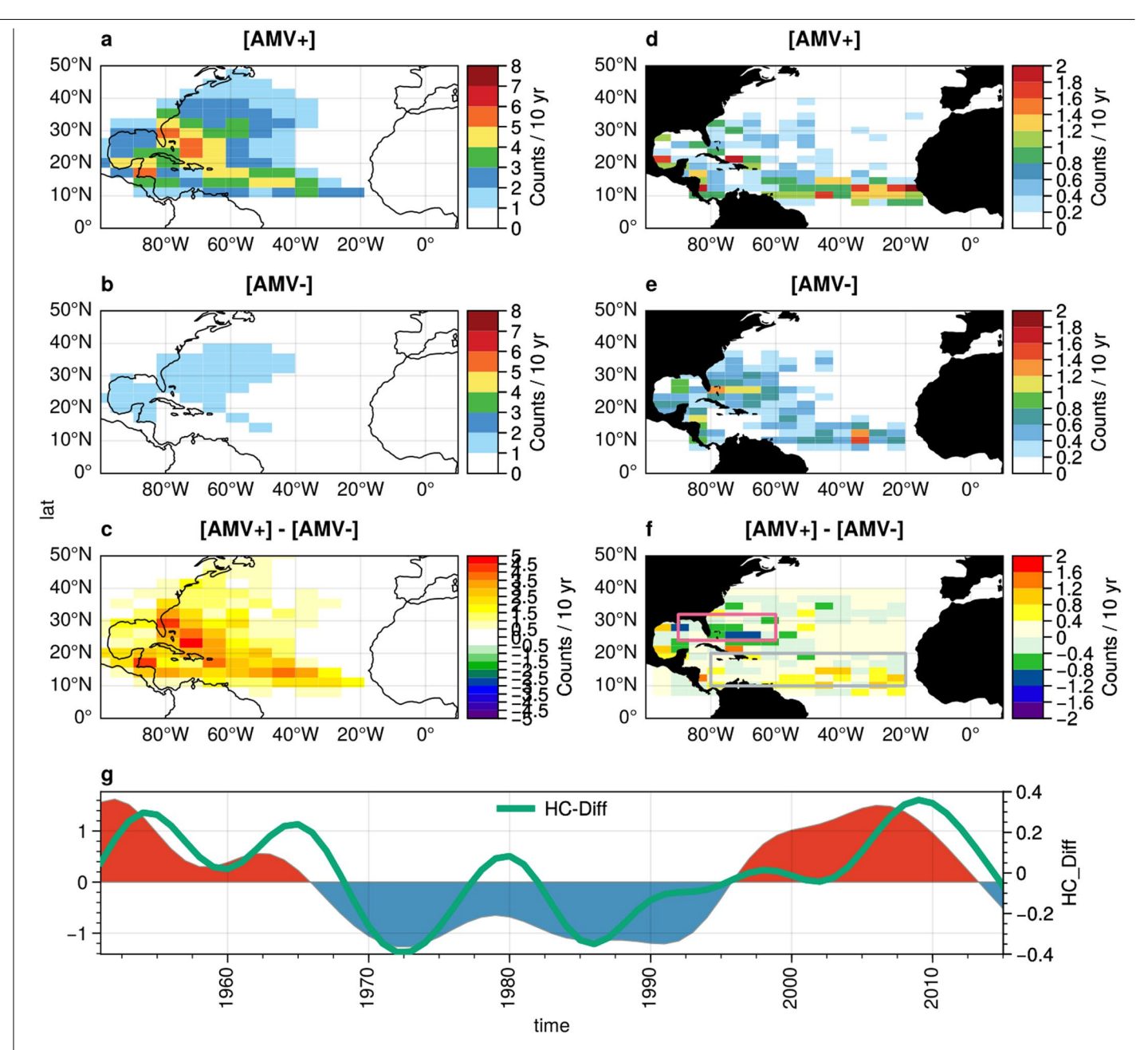
Extended Data Fig. 1 | Model-data Northern Hemisphere rainfall difference due to inter-hemispheric SST contrast difference. a, JJASO precipitation trend difference between CMIP6 and GPCC over land in 1950–2014. b, as in a but for the difference between CMIP6 and 20th reanalysis. c, regression of precipitation difference (CMIP6 – GPCC) on the inter-hemispheric SST contrast difference (gray curve in Fig. 1e). d, as in c but for precipitation difference

 $(CMIP6-20^{th}\,rean alysis).\,In\,\textbf{d}, the\,black\,curve\,is\,the\,location\,of\,maximum\,rainfall\,climatology\,in\,20^{th}\,rean alysis.\,Note\,that\,unlike\,in\,Fig.\,1a-c, the\,precipitation\,time\,series\,here\,are\,not\,normalized.\,Regions\,of\,statistical\,significance\,at\,the\,99\%\,confidence\,level\,according\,to\,Student's\,t\,test\,are\,hatched.\,Maps\,are\,plotted\,using\,the\,cartopy\,package\,in\,Python.$



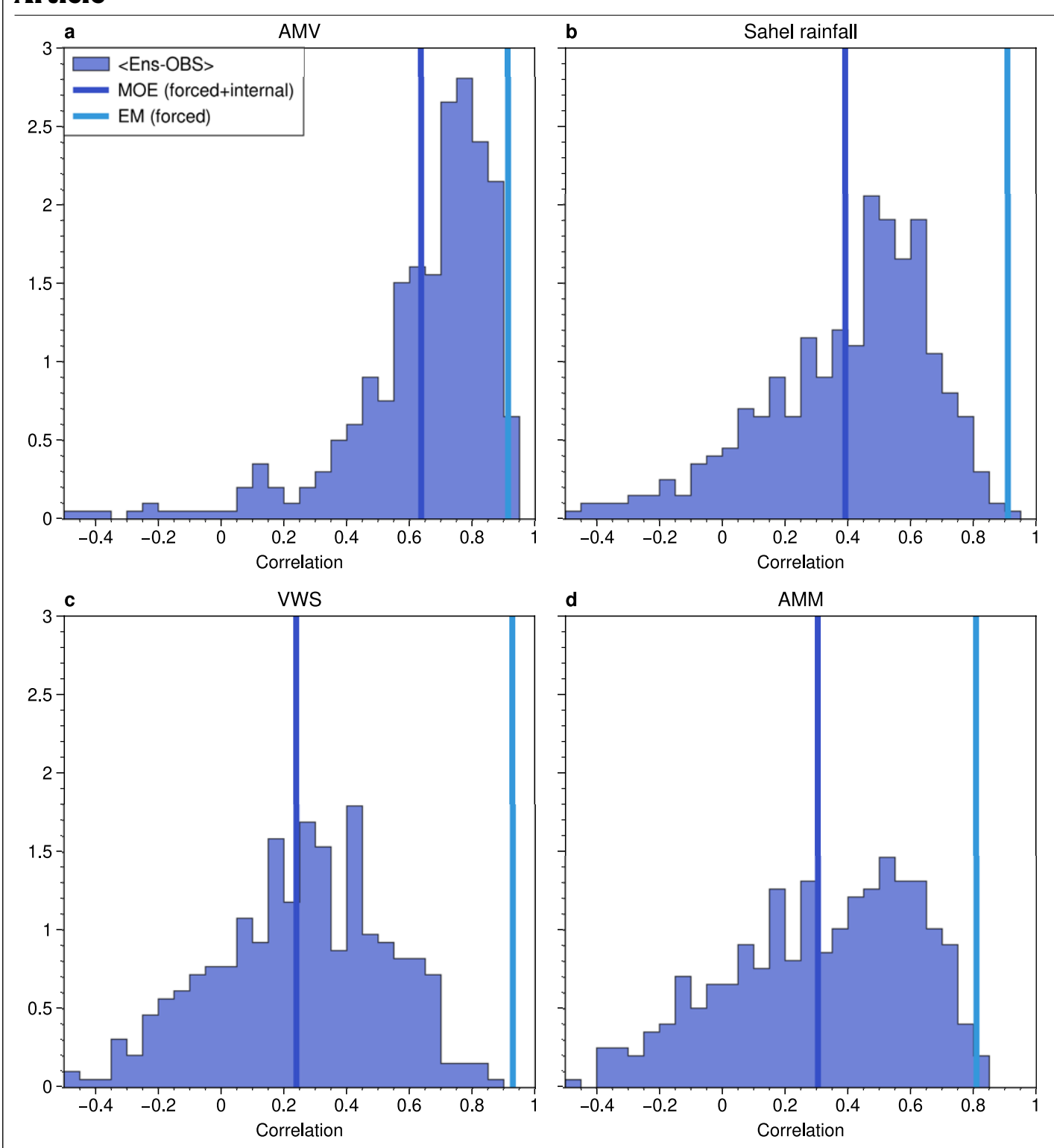
Extended Data Fig. 2 | SST trends in models and observations in 1950-2014. a, JJASO SST trend in runs forced by anthropogenic aerosols from DAMIP. b, as in a but for greenhouse gases. c, as in a but for natural forcings. d, the sum of a-c. e, as in a but for all forcing from CMIP6. f, as in e but for observation.

Regions of statistical significance at the 99% confidence level according to Student's t test are hatched in $\mathbf{a}-\mathbf{f}$. Maps are plotted using the cartopy package in Python.



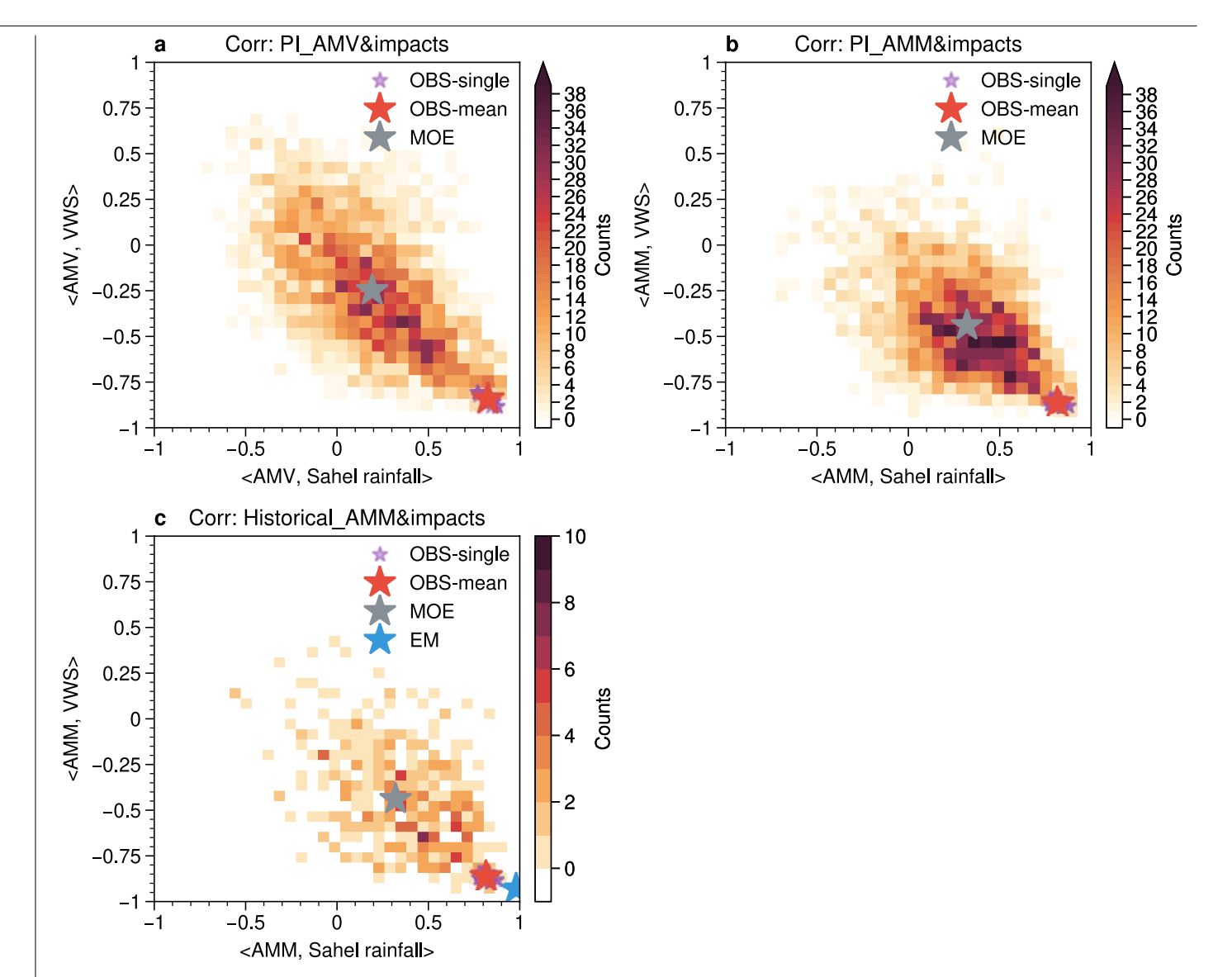
Extended Data Fig. 3 | **North Atlantic Hurricane associated with the AMV. a**, hurricane track density in positive AMV. **b**, as in **a** but for negative AMV. **c**, the difference between **a** and **b**. **d**, hurricane genesis density in positive AMV. **e**, as in **d** but for negative AMV. **f**, the difference between **d** and **e**. **g**, normalized hurricane frequency (shading) as in Fig. 2c and ratio difference between

hurricane generated over main development region $[10-20^\circ\text{N}, 80-20^\circ\text{W}]$ and over Bermuda Sea $[24-32^\circ\text{N}, 90-60^\circ\text{W}]$ (green curve, right y-axis). In \mathbf{f} , the main development region is marked as gray box, and the Bermuda Sea is pink box. Maps are plotted using the cartopy package in Python.



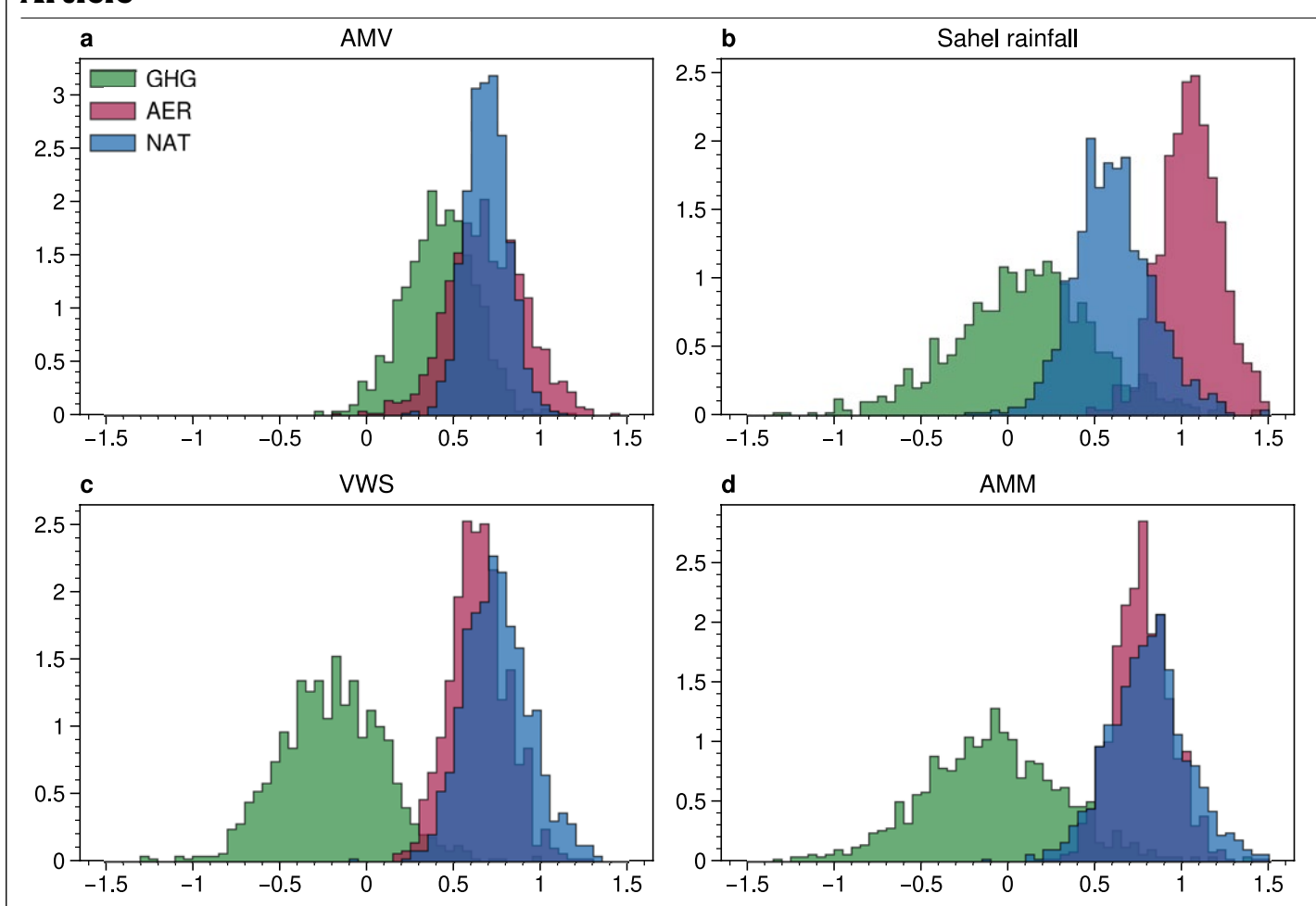
Extended Data Fig. 4 | **Correlations between simulations and observations. a**, correlation distribution between simulated AMVs and the observed AMV.
The dark blue line is the mean of the distribution (MOE). The light blue line is

the correlation between the forced AMV (EM) and observation. b-d , as in a but for Sahel rainfall, VWS, and AMM.

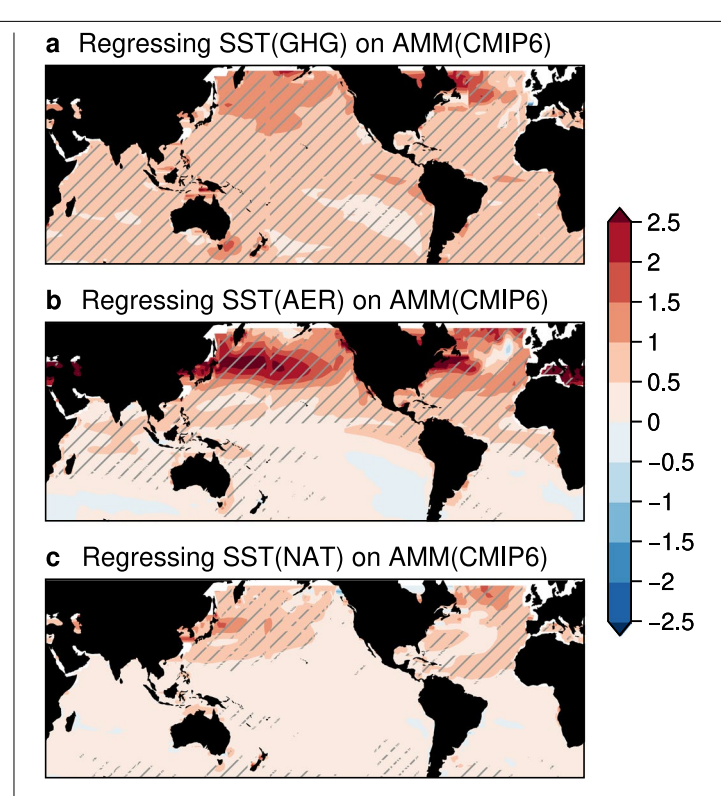


Extended Data Fig. 5 | Correlations between AMV/AMM and Sahel rainfall and VWS in preindustrial and historical runs (1950–2014). a, joint distribution of correlations between the AMV and VWS (y-axis) and Sahel rainfall (x-axis) in preindustrial runs (N = 3100) and observation (red star). b, as in a but for AMM. c, as in b but for historical runs (with forced response included in single realizations). Comparing panel a and b shows the AMM has a better correlation

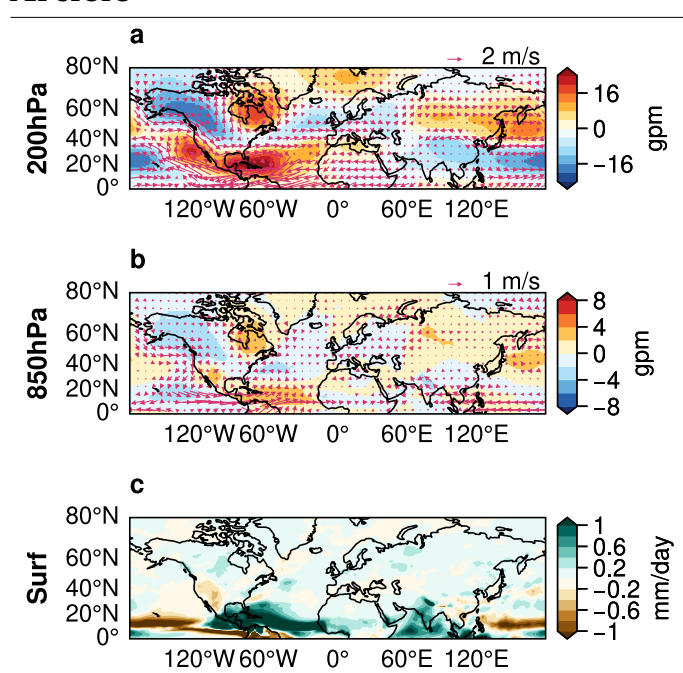
with Sahel rainfall and VWS than AMV. Similar conclusion could also be drawn by comparing panel \mathbf{c} and Fig. 2e. Comparing panel \mathbf{c} and Fig. 4b shows the shift of observation before and after 1950. The small purple stars under the big red star are correlations calculated using different datasets, so the red start is the average of the purple stars. See methods how the correlations are calculated.



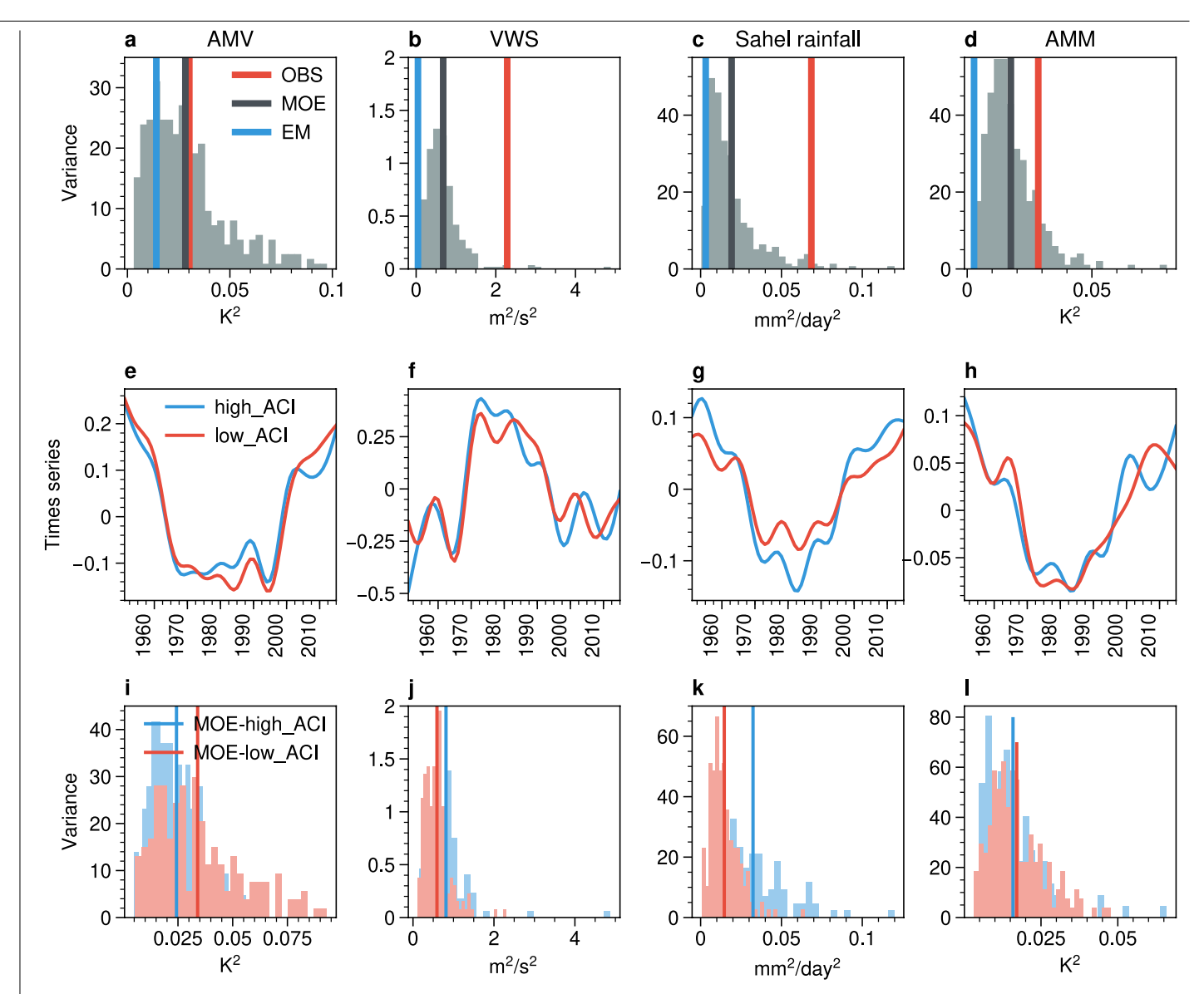
 $\textbf{Extended Data Fig. 6} | \textbf{Distribution of regression coefficients by regressing detrended and lowpassed all-forcing run on single-forcing runs in bootstrap.} \\ \textbf{a}, \textbf{AMV. b}, \textbf{Sahel rainfall. c}, \textbf{VWS. d}, \textbf{AMM}. \\ \textbf{a}, \textbf{AMM. d}, \textbf{AMM.} \\ \textbf{b}, \textbf{Candidate of the property o$



 $\label{lem:extended} \textbf{Data} \ \textbf{Fig.} \ \textbf{7} \ | \ \textbf{Regression} \ \textbf{of} \ \textbf{SST} \ \textbf{from} \ \textbf{single} \ \textbf{forcing} \ \textbf{run} \ \textbf{on} \ \textbf{AMM} \\ \textbf{from} \ \textbf{all-forcing} \ \textbf{CMIP6} \ \textbf{run.} \ \textbf{a}, \ \textbf{greenhouse} \ \textbf{gases.} \ \textbf{b}, \textbf{c}, \ \textbf{as} \ \textbf{in} \ \textbf{a} \ \textbf{but} \ \textbf{for} \\ \textbf{anthropogenic} \ \textbf{aerosols} \ \textbf{and} \ \textbf{natural} \ \textbf{forcings.} \ \textbf{Regions} \ \textbf{of} \ \textbf{statistical} \\ \textbf{significance} \ \textbf{at the} \ \textbf{99\%} \ \textbf{confidence} \ \textbf{level} \ \textbf{according} \ \textbf{to} \ \textbf{Student's} \ \textbf{test} \ \textbf{are} \\ \textbf{hatched.} \ \textbf{Maps} \ \textbf{are} \ \textbf{plotted} \ \textbf{using} \ \textbf{the} \ \textbf{cartopy} \ \textbf{package} \ \textbf{in} \ \textbf{Python.} \\ \\ \ \textbf{Python.} \\ \\ \ \textbf{and } \ \textbf{an$



Extended Data Fig. 8 | **Response of tropical North Atlantic heating in CESM-SOM. a**, 200hPa geopotential height and circulation. **b**, as in **a** but for 850hPa. **c**, precipitation. The 200hPa (850hPa) response is averaged between 150–250hPa (700–900hPa) on native hybrid-pressure model level. Maps are plotted using the cartopy package in Python.



Extended Data Fig. 9 | **Signal-to-noise paradox in the CMIP6 models. a**, distribution of the post-1950 AMV variance for ensemble member (gray), forced response (EM, blue), total response of model (MOE, black), and observation (red). **b**, **c**, **d** as in **a**, but for VWS, Sahel rainfall, and AMM. **e**, ensemble mean of AMV in models with strong aerosol-cloud interaction (blue) and weak aerosol-cloud interaction (red). **f**, **g**, **h** as in **e**, bur for VWS, Sahel rainfall, and AMM. **i**, distribution of the post-1950 AMV variance in models with strong aerosol-cloud interaction (blue) and weak aerosol-cloud interaction (red). **j**, **k**, **l** as in **i**, but for VWS, Sahel rainfall, and AMM. In **e-l**,

models are divided into two composites based on the strength of aerosol forcings ¹⁹. Models with strong aerosol forcings are represented in blue and they are: TaiESM1, CESM2-FV2, SAM0-UNICON, CESM2-WACCM, CESM2-WACCM-FV2, CESM2, NorESM2-LM, NorESM2-MM, ACCESS-CM2, CNRM-CM6-1, MIROC6. Models with weak aerosol forcings are represented in red, and they are: GFDL-ESM4, MIROC-ES2L, BCC-CSM2-MR, CNRM-ESM2-1, GFDL-CM4, CanESM5, EC-Earth3-Veg, IPSL-CM6A-LR, BCC-ESM1, FGOALS-g3, MPI-ESM1-2-HR, MPI-ESM1-2-LR, INM-CM4-8, CAMS-CSM1-0.

Extended Data Table 1 | a, variance and signal-to-noise ratio of the pre- and post-1950 AMV, VWS, Sahel rainfall, and AMM in CMIP6 models. b, variance of observed AMV, VWS, Sahel rainfall, and AMM in the pre- and post-1950 period

a	Model	Pre-1950 (non	Pre-1950 (detrending)	Post-1950
		detrending)	ζ,	(detrending)
AMV	MOE	0.0205	0.0114	0.0283
	EM	0.0055	0.0011	0.0141
	IV	0.0150	0.0103	0.0142
	S/N ratio	0.3686	0.1107	0.9959
Sahel	MOE	0.0130	0.0119	0.0192
Rainfall	EM	0.0005	0.0005	0.0031
	IV	0.0125	0.0114	0.0160
	S/N ratio	0.0413	0.0461	0.1965
VWS	MOE	0.5314	0.4937	0.6794
	EM	0.0079	0.0088	0.0459
	IV	0.5235	0.4848	0.6335
	S/N ratio	0.0150	0.0182	0.07
AMM	MOE	0.0162	0.0135	0.0175
	EM	0.0010	0.0007	0.0027
	IV	0.0152	0.0128	0.0148
	S/N ratio	0.0626	0.0524	0.1862
b	Observation	Pre-1950 (non	Pre-1950 (detrending)	Post-1950
		detrending)		(detrending)
AMV	COBE2	0.0657	0.0157	0.0354
	ERSSTv5	0.0790	0.0166	0.0265
	HadiSST	0.0468	0.0141	0.0287
	Mean	0.0638	0.0155	0.0302
Sahel	CRU	0.0159	0.0111	0.0699
Rainfall	GPCC	0.0217	0.0211	0.0628
	UDEL	0.0190	0.0182	0.0728
	Mean	0.0189	0.0168	0.0685
VWS	20th reanalysis	0.8850	0.8694	1.1141
	NCEP reanalysis 1			3.4592
	Mean	0.8850	0.8694	2.2867
AMM	COBE2	0.0178	0.0174	0.0268
	ERSSTv5	0.0327	0.0233	0.0298
	HadiSST	0.0142	0.0111	0.0289
	Mean	0.0216	0.0173	0.0285

Note for the pre-1950 AMCV, we calculate the variance and signal-to-noise ratio using both non-detrended and detrended time series. The results indicate that they are similar, except for the non-detrended AMV which exhibits a higher variance due to an increasing trend in the early period (Fig. 4d). In **a**, the signal-to-noise ratio in the model for the pre-1950 period is much lower compared to the post-1950 ratio. In **b**, the observed variance in the pre-1950 period is lower compared to the post-1950 period, which is primarily driven by external forcing. This indicates that the pre-1950 AMCV is more influenced by internal variability. Units for AMV, AMM, SPR, and VWS variances are °C², °C², mm²/day² and m²/s², respectively.